RESEARCH PAPER



Multiscale analysis of rotational penetration in shallow dry sand and implications for self-burrowing robot design

Yong Tang¹ · Junliang Tao¹ ©

Received: 16 July 2021 / Accepted: 4 February 2022 © The Author(s), under exclusive licence to Springer-Verlag GmbH Germany, part of Springer Nature 2022

Abstract

In nature, seeds of some flowering plants such as *Erodium and Pelargonium* can bury themselves into the ground effectively for germination. Jung et al. (Phys Fluids 29:041702. https://doi.org/10.1063/1.4979998, 2017) hypothesized that rotation induced by the hygroscopic coiling and uncoiling movement of the awn reduces the penetration resistance. Rotational penetration was also studied in geotechnical engineering, as it is relevant to the rotary installation of piles. However, there are limited fundamental explanations of the effect of rotation on the reduction of penetration resistance. In this study, shallow rotational penetration in dry sand is studied using the discrete element method (DEM); the directly available particle-scale data and the derived meso-scale data were analyzed to reveal the underlying mechanism of the rotational effect on penetration. A series of rotational penetration tests with different rotational speeds were conducted. It was confirmed that the penetration resistance at the cone decreases with rotational speed. Analysis of the particle-cone contact data shows that rotation does not only result in the inclination of the contact forces, but also significantly reduces their magnitude and the overall contact number. The force chain network, displacement fields and particle trajectories visualize the rotational effects at the particle-scale; and the evolution of the principal stresses of the soil provides a meso-scale explanation. The new multi-scale data tested the "force chain breakage" hypothesis and challenged the assumptions previously used in developing analytical models. Insights were also provided to power consumption and implications on the design of a self-burrowing robot, which could take advantage of the rotational effect on penetration.

Keywords Bio-inspired · Burrowing robot · Discrete element method · Penetration · Power · Rotation

List of symbols		θ	The contact angle between the positive z axis
α	Semi-angle of the cone (°)		and the resultant contact force on the cone (°)
α_s	Shear to normal stiffness ratio	ϑ	Rotational angle of the shear stress (°)
β	Rolling stiffness coefficient	ω	Rotational velocity (radian/s)
δ	Angle of soil–penetrator friction (°)	n	Sample initial porosity
η	Plastic moment coefficient	σ	Stress normal to the cone surface (kPa)
$ heta_i$	The contact angle between the positive z axis	$c_{\rm a}$	Soil-penetrator adhesion (kPa)
	and the contact force at contact i (°)	CN	Contact number
$ heta_{ m r}$	Rotational angle between two contacting par-	$D_{ m c}$	Diameter of the cone (m)
	ticles (°)	$D_{ m s}$	Diameter of the shaft (m)
		F	Total contact force on the penetrator (N)
		$\parallel F_{\mathrm{n}} \parallel$	Normal value of the normal contact force (N)
		$F_{\rm z}$	The vertical component of the total contact
			force on the penetrator (N)
		$F_{\rm zn}$	Vertical component of the total contact normal
Yong Tang			force on the penetrator (N)
ytang i	16@asu.edu	F_{zt}	Vertical component of the total contact shear
1 School	of Sustainable Engineering and the Built		force on the penetrator (N)
Geotecl	nment, Center for Bio-Mediated and Bio-Inspired hnics, Arizona State University, 650 E Tyler Mall, AZ 85287, USA	F_{zi}	Individual contact forces on the penetrator (N)

Published online: 08 March 2022

F_{zc}	Vertical component of the total contact normal
	force on the cone (N)
$F_{\rm zs}$	Vertical component of the total contact shear
	force on the shaft (N)
$F_{\text{zn}i}, F_{\text{zt}i}$	Vertical components of the individual contact
	normal forces and that of the contact shear
	forces (N)
$F_{\rm znc}, F_{\rm ztc}$	Vertical component of the contact normal force
	and contact shear force on the cone (N)
$H_{\rm s}$	Height of the shaft (m)
$k_{\rm r}$	Rolling stiffness coefficient
$k_{\rm s}$	Tangential (shear) contact stiffness (kPa)
M_{e}	Elastic contact moment (N m)
$M_{\rm p}$	Plastic contact moment (N m)
n_p	Cone-to-particle diameter ratio
$\stackrel{r}{P}$	Power (W)
$q_{\rm c}$	Cone penetration resistance (kPa)
$q_{\rm cmax}$	Non-rotational cone penetration resistance at
Temm	the maximum penetration depth (kPa)
$q_{ m cRot}$	Rotational cone penetration resistance (kPa)
Q	Vertical penetration force (N)
Q_c, Q_s	(Vertical components of) the penetration force
20, 20	acting on the cone and shaft (N)
$r_{\rm a}, r_{\rm b}$	Radii for two contacting particles (m)
$r_{ m d}$	Chamber-to-cone diameter ratio
R	Radius of the cone (m)
T	Penetration torque or the total contact torque
	on the penetrator (N m)
T_{p}	Rotational period (s)
$T_{\rm z}^{\rm P}$	The vertical component of the total contact
L	torque (N m)
$T_{\rm zc}, T_{\rm zs}$	Vertical components of the torque on the cone
EC / ES	and shaft (N m)
и	Relative slip velocity
$v_{\rm p}$	Vertical penetration velocity (m/s)
$v_{\rm s}$	Tangential velocity (m/s)
S	

1 Introduction

Bio-inspired geotechnics, as a subfield of the emerging subject field of biogeotechnics, concerns how geotechnical engineers can learn from biological solutions to improve the sustainability, resilience and sophistication of the tools and methods in geotechnical practice [26, 39]. One particular topic of bio-inspired geotechnics, penetration/burrowing mechanisms and robots, has gained much traction recently [8, 26, 36, 39, 54, 62]. It is envisioned that self-burrowing robots can be used for exploration, search-and-

rescue, sensor deployment, inspection, monitoring, surveillance, transport, and construction purposes [53].

Numerous organisms move in soil effectively and efficiently. Examples include burrowing bivalves, polychaetes, earthworms, burrowing fish, sandfish lizards, and tree roots [3, 17, 37, 41, 45, 51, 55–57]. They achieve this by using a spectrum of traits but mainly through changing their body shapes so as to decrease the penetration resistance or to increase the thrust and anchorage. Many of these traits have also been investigated to inspire the design of self-burrowing robots [18, 38, 40, 43, 46, 54, 60]. This study is inspired by the self-burial mechanism of some flowering seeds.

It has been found that the seeds of Erodium cicutarium and Pelargonium species can bury themselves into the ground by cyclically alternating the coiling and uncoiling motion of its awn structure [21, 22, 50]. In general, the awn is a bristle-like appendage on the seeds. Elbaum and Abraham [1, 2, 19, 20], among others, found that the awn has a bilayered structure, which includes a hygroscopically contracting inner layer and a stiffer outer layer. Humidity changes cause the double-layer structure to deform in a non-uniform fashion, resulting in a coiling and uncoiling motion. This periodical process leads to a rotational penetration movement of the seed. As a result, seeds bury themselves into the ground for future germination. It is believed that the net penetration thrust originates from the asymmetric kinematics of the helical motion [15], and the penetration resistance is also reduced by the rotational motion [31, 52]. Specifically, Jung et al. [30] experimentally investigated the rotational movement of the seeds of the *Pelargonium* species. By penetrating a seed analog into a rotating container full of glass beads, the penetration resistance decreased up to 75% at a rotation rate of 7 rpm and a vertical velocity of 0.2 mm/s as compared to the case without rotation. They developed a mathematical model to empirically correlate the penetration resistance with the relative slip velocity (i.e., the ratio between the slip velocity and the penetration velocity) of the grains. They hypothesized that the rotation of the intruder induces additional interparticle movements, which facilitate the breaking of the force chains around the penetrator, thereby reducing the vertical penetration forces. Bengough et al. [7] also investigated the effect of rotation on frictional and total penetration resistance to understand why the friction portion of the resistance force of a penetrator probe is much larger than that on a plant root. They conducted penetration tests, with or without rotation, in different soil types. It was hypothesized that the rotation altered the orientation of the vector of frictional resistance so that it reduced the total penetration resistance [7]. Assuming that the soil is homogeneous and the stress normal to the cone surface is not affected by rotation, a theoretical model was developed



to include the effect of rotation period and penetration rate in the estimation of penetration resistance [7].

Although macroscopic continuum or empirical models have been developed to reflect the effect of rotation on penetration resistance, a mechanistic explanation at the micro (particle) and meso (stress/strain) levels is necessary to unveil the fundamental mechanisms. In this context, discrete element method (DEM) is an ideal tool. In fact, Sharif et al. [47] recently investigated the effects of the installation pitch (the ratio between rotational and vertical velocity, the same as relative slip ratio) and base geometry on the installation requirements of rotary installed piles using DEM. But their objective was to develop a prediction method based on the cone penetration test; only limited insights on the microscopic behavior were provided. This study aims to complement the above works by providing a "micro to macro" DEM data analysis of shallow rotational penetration of a rod in dry cohesionless soil; the force, torque, and power involved in rotational penetration were also examined to offer implications for the design of selfburrowing robots.

This paper starts with an overview of the simulation and analysis methodologies, including the numerical methods, model construction, and data analysis approaches. Subsequently, the simulation results, including the particle–penetrator interface contact information, force chain network, displacement field, and particle trajectory, are analyzed to elucidate the reduction of the penetration resistance. A detailed discussion on the fundamental mechanisms is then presented, followed by implications for robot design and some conclusions based on the results of this study.

2 Methodology

The DEM method has been used to simulate different soil—structure interaction problems, such as the cone penetration test [9], screw pile installation [48], and general soil—structure interface behavior [29]. Recently, DEM method was also used to investigate the soil—organism interactions [38], and soil—robot interactions [11, 26, 36]. Nevertheless, the DEM method still cannot handle these sophisticated engineering problems on a real physical scale due to the computational limitations. Therefore, some simplifications—such as increasing the critical timestep, using upscaled spherical particles, and adopting simple constitutive laws—are usually made to reduce computational costs without significantly reducing the computational accuracy.

2.1 Numerical method

This study uses the open-source software YADE [49] to investigate the soil-penetrator interactions. In YADE, the kinematics of the particles is controlled by Newton's second law of motion and the constitutive relationship between particle force and displacement. In this study, the sand particles are simplified as spherical balls. A built-in linear elastic-plastic constitutive model (Cundall-Strack law) is used to describe the interactions between any two contacting particles. The contact shear failure criterion used here follows the Mohr-Coulomb law. Besides, a moment transfer law [6] was introduced to account for the effects of sand particles' roughness and angularity. More information on this law [6, 44, 61] can be found in the "Appendix", while the detailed information on the DEM theory is not duplicated here and can be found elsewhere [49, 52, 61].

2.2 Model construction and microscopic parameters

A virtual calibration chamber was constructed with key geometric considerations [4, 10], including the particle size distribution, cone-to-particle diameter ratio (n_p) , the chamber-to-cone diameter ratio (r_d) , and the sample height-to-cone diameter ratio (n_h) . The particle size distribution was based on that of the Ottawa F65 but scaled up by 25 times (Fig. 1a). Sample parameters in this study (Table 1) were selected as a compromise between the available computational power and the simulation accuracy. Specifically, the height and diameter of the sample are 0.25 m and 0.4 m (Fig. 1b); the penetrator consists of a cylindrical shaft with a length of 0.15 m and a diameter of 0.025 m; a conical tip with a semi-angle of 30° connects to the bottom of the shaft (Fig. 1c). The justification of the selection of these geometry ratios are provided in the "Appendix". When implementing in YADE, the cross section of the penetrator was approximated with a regular decagon (a polygon with ten equal sides) with an equivalent diameter of 0.025 m.

The microscale parameters (Table 1) were calibrated to match the experimental triaxial compression stiffness and peak strength of dry Ottawa F65 samples [5, 58]. Details of the calibration process and results can be found in Tang et al. [52]. The calibrated and validated curves for deviatoric stress-axial strain and volumetric strain-axial strain were shown in the "Appendix" for convenience.

The sample for the rotational penetration simulations was prepared using a multi-step tuning approach. A loose sample was first generated using a "pluviation" method within the frictionless cylindrical calibration chamber



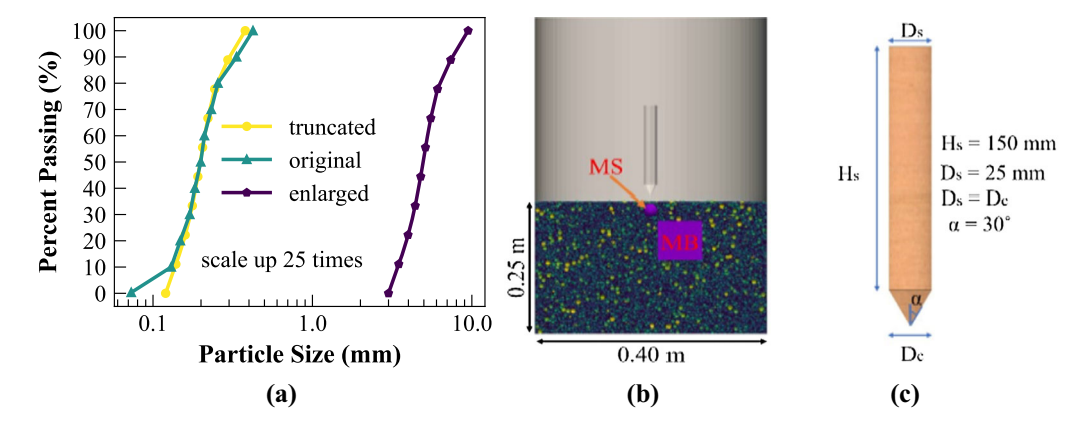


Fig. 1 Simulation setup: **a** original and scaled particle size distribution curves; **b** penetration test chamber geometry: the colors of the sample represent the magnitude of the particle radii; the relative positions of the monitoring sphere (MS; D = 0.025 m) and the measurement box (MB; L = 0.075 m) are also shown; before penetration, the penetrator tip is located 0.01 m above the sample surface; **c** the penetrator model and its dimensions

Table 1 Key sample and microscale parameters for the Ottawa sand F65 sample

Parameters	Values
Sample height (mm)	250
Sample diameter (mm)	400
Number of particles	367,000
Sample porosity (n)	0.412
Particle density (kg/m ³)	2,648
Acceleration of gravity (m/s ²)	9.81
Interparticle friction angle (°)	19.5
Penetrator-particle friction angle (°)	19.5
Young's modulus (MPa)	400
Ratio of shear to normal stiffness (α_s)	0.3
Plastic moment coefficient (η)	0.5
Rolling stiffness coefficient (β)	0.2

using a high initial interparticle friction angle (45°). The targeted porosity was then achieved by gradually reducing the interparticle friction angle. Following this process, the friction angle was reset to the calibrated value after the unbalanced force decreased to 0.001 N, ensuring that the sample was in the quasi-static equilibrium. Afterwards, some particles on the top were removed to ensure a flat surface. The samples were then rerun to achieve a final equilibrium state. The penetrator was initially generated so that the tip was located at 0.01 m above the top surface of the sample (Fig. 1b).

Five cases were conducted with a common vertical penetration velocity (0.04 m/s) but different rotational velocities (0, 40, 100, 200, and 400 rpm). The rotation of the penetrator was realized by assigning a rotational velocity in the horizontal plane around the penetrator's

central axis. In addition, since this study concerns shallow penetration, gravity was considered.

2.3 Data analysis

Figure 2 presents the schematic for the contact force between the cone and a contacting sphere. From a particle-scale perspective, the vertical penetration force (Q) includes contributions from the contact normal force (F_{zn}) and the contact shear force (F_{zt}) , as shown in Eq. (1).

$$Q = F_{zn} + F_{zt} = \sum_{i=0}^{CN} F_{zni} + \sum_{i=0}^{CN} F_{zti}$$
 (1)

From a macro-scale perspective, Q can be seen as the sum of the vertical components of the resultant contact forces (F_{zi}) , which depend on the magnitudes of the forces (F_i) and the contact angles (θ_i) as defined in reference to the positive z direction (Eq. 2).

$$Q = \sum_{i=0}^{\text{CN}} F_{zi} = \sum_{i=0}^{\text{CN}} F_i \cdot \cos\theta$$

$$\cos\theta_i = \frac{F_{zi}}{F_i} = \frac{F_{zi}}{\sqrt[2]{F_{\text{n}i}^2 + F_{ti}^2}}$$
(2)

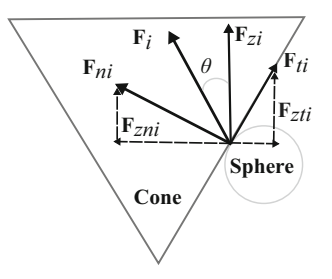


Fig. 2 Schematic for the contact force components between the cone and the contacting spheres



Alternatively, Q can also be viewed as the sum of contributions from the forces acting on the cone (Q_c) and shaft (Q_s) .

$$Q = Q_{\rm c} + Q_{\rm s} = F_{\rm zc} + F_{\rm zs} \tag{3}$$

where Q_c and Q_s are the vertical penetration forces acting on the cone and shaft, respectively; F_{zc} and F_{zs} are the vertical components of the total contact forces on the cone and shaft, respectively.

The rotational movement generates torque on the penetrator and consumes energy during the penetration process. The total power consumption (P), or the energy consumption per unit time, can be expressed as the sum of contributions from vertical components of the penetration force $(F_z = Q)$ and torque (T_z) . The power is a key performance metric for robot design, and it can be expressed as,

$$P = Q \times v_{p} + T_{z} \times \omega = (Q_{c} + Q_{s}) \times v_{p} + (T_{zc} + T_{zs}) \times \omega$$
(4)

where $T_{\rm zc}$ and $T_{\rm zs}$ are the vertical components of the torques acting on the cone and shaft, respectively; $v_{\rm p}$ and ω are the vertical velocity and rotational velocity, respectively.

In addition, a measurement sphere (D = 0.025 m) and a measurement box (L = 0.075 m) are used to monitor the trajectory of select particles and the meso-scale principal stress in the sample during the penetration process (Fig. 1b). The sizes of the measurement sphere and box are large enough to serve as representative volume elements and are within the range of commonly adopted values (Table 2).

The underlying mechanism of rotation effect on penetration resistance can be explained by examining the changes of the multi-scale terms in Eqs. (1)–(3) and by relating to the particle-level displacements, trajectories,

Table 2 The ratio between the measurement sphere and the average particle diameter in the literature

Model	Measurement sphere diameter <i>D</i> (mm)	Particle Diameter D_{50} (mm)	D/D_{50}	References
3D	20	4.2	5	[35]
3D	20	1.984	10.1	[14]
3D	300	51	5.9	[27]
3D	180	41	4.4	[24]
3D	3000	540-660	4.5-5.5	[12]
3D	36	8.91	4	[13]
3D	104	4.6-5.2	20-22.6	[59]
2D	180	7.6	23.7	[28]
2D	10.0-50.0	3.0-4.0	3.3-16.6	[32]
2D	20–30	0.78	25.6–38.5	[34]

force chains and changes of meso-scale principal stresses. Each of these aspects are discussed in Sect. 3.

3 Results

3.1 Macro-scale resistive force and torque on the cone and shaft

The penetration forces on the cone (Q_c) and shaft (Q_s) are shown in Fig. 3. Q_c increases with increasing penetration depth and decreases with the rotational speed, while Q_s contributes much less to the total penetration force (less than 10% of Q_c for the control case). Although differences in Q_s exist among cases, there is no obvious trend due to the coarseness of data (Fig. 3b).

Rotational movement reduces the penetration force with a cost related to torque (Fig. 4). Theoretically, there should be no torque for the control case if the sample is a homogenous continuum medium. However, as shown in Fig. 4, a net torque exists on the cone and shaft for the penetrator with a pure downward motion (0 rpm). This observation implies that the original sample is not homogenous, and the components of the contact forces on the *xy* plane do not balance off. Figure 4a shows that a faster speed of the cone actually does not result in higher torque since higher rotational speed significantly reduces the particle—cone contact forces and numbers. For the shaft (Fig. 4b), the differences among the rotational cases are not obvious.

Note that the calculated torque is likely overestimated, since the surface of the penetrator is not perfectly round, but a ten-sided polygon. The authors also constructed models with polygons of higher number of sides to approximate a perfect round cross section. The results (see "Appendix") indicate that the cone penetration force only increases slightly with the increase in the number of sides, while the shaft resistive force does not show any clear trend.

3.2 Contact number at the particle-penetrator interface

The penetration forces (Q_c and Q_s) are affected by the number of particles that contact the cone and shaft (Eqs. 1, 2). Figure 5 summarizes the evolution of the number of particle–cone and particle–shaft contacts under different rotational velocities. During the penetration process, the particle–cone contact number increases sharply until the cone is fully submerged (penetration depth of 0.025 m). After that, the particle–cone contact number maintains at a relatively constant value with some fluctuations. The average particle–cone contact number is 34 for the control



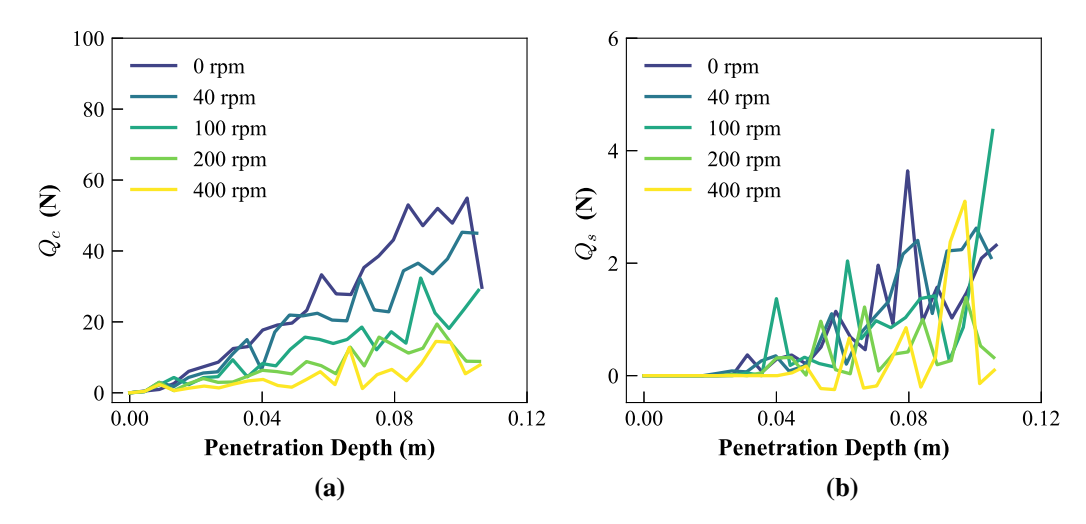


Fig. 3 Penetration force under different rotational velocities: \mathbf{a} cone penetration force (Q_c) ; \mathbf{b} shaft penetration force (Q_s) . Note that the scales for the vertical axis are different for \mathbf{a} and \mathbf{b}

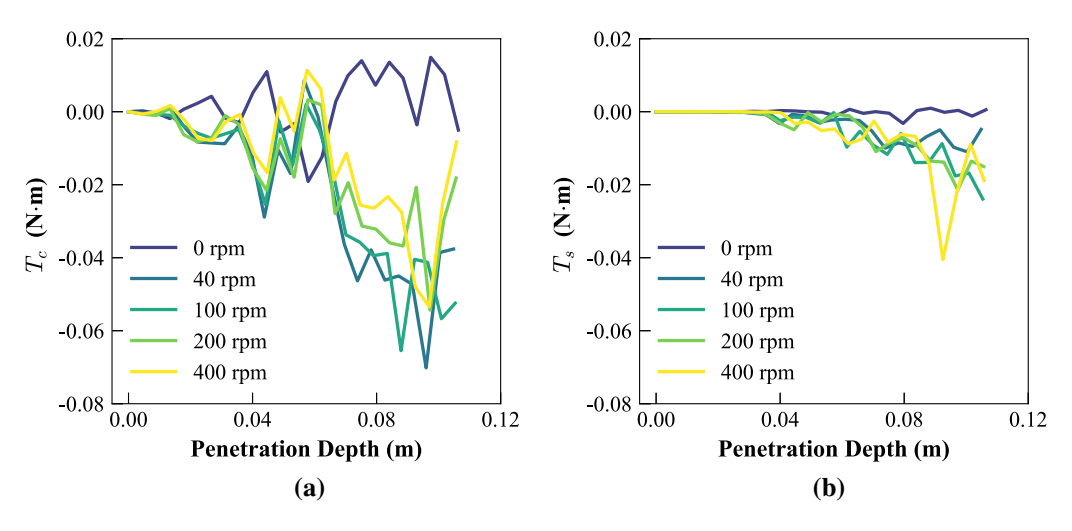


Fig. 4 Torque under different rotational velocities: a torque on the cone; b torque on the shaft

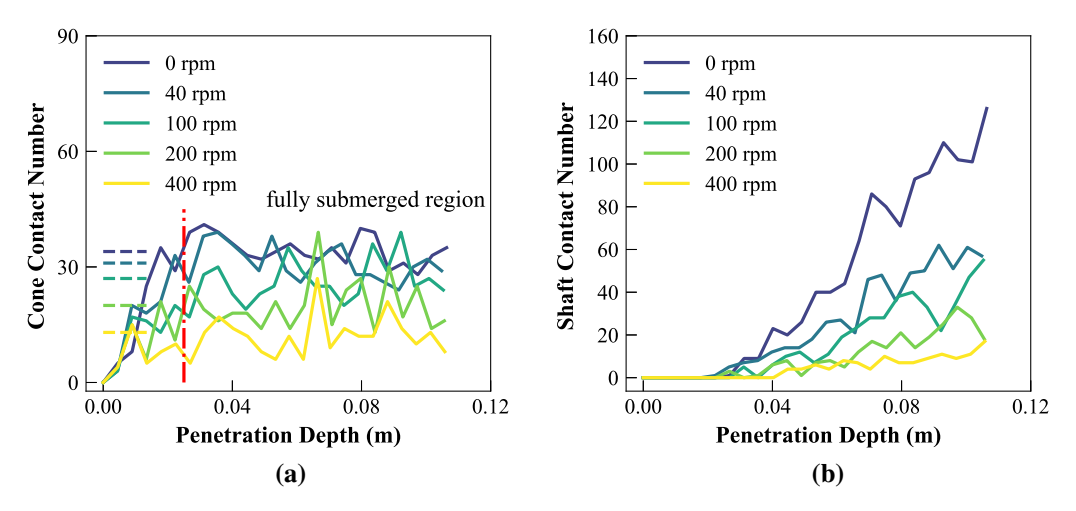


Fig. 5 Contact number (CN) under different rotational velocities: a contact number on the cone (the red dash-dot line indicates the fully submerged region); b contact number on the shaft



case (0 rpm), while that for 400 rpm is only 13. The particle–shaft contact number (Fig. 5b) increases almost linearly with the increase of the penetration depth for all cases mainly due to the increase in the length of shaft that is submerged. The stabilized average contact number (dash–dotted line in Fig. 5a) and the particle–shaft contact number both decrease with increasing rotational speed.

3.3 Magnitude and components of the contact forces at the particle-penetrator interface

The total cone penetration force is the sum of vertical contributions from the normal $(F_{\rm znc})$ and shear $(F_{\rm ztc})$ contact forces (Eq. 1). From Fig. 6, both $F_{\rm znc}$ and $F_{\rm ztc}$ increase with increasing penetration depth but decrease with the rotational velocity. During the penetration process, the $F_{\rm znc}$ contributes more to the cone penetration force when compared to the $F_{\rm ztc}$ under the same rotational velocity. When the rotational velocity is large enough (above 200 rpm), the $F_{\rm ztc}$ on the cone becomes negligible.

Figure 6 shows that the relative reduction of the cone penetration force are not linear with respect to the rotational velocity but increases with the rotational velocity, although the reduction rate decreases. For example, the relative reduction of F_{zc} (or Q_c) from 40 to 100 rpm is almost the same as the reduction from 200 to 400 rpm; both are around 20%.

The total cone penetration force can also be expressed as a resultant contact force with a corresponding contact angle (Eq. 2). The evolutions of the resultant contact force and contact angle on the cone during the penetration process are shown in Fig. 7. The resultant contact force increases with penetration depth and decreases with the rotational velocity; the stabilized contact angle (after the cone is fully

submerged) increases with the rotational velocity. The maximum contact angle is around 60°, which is the same as the apex angle of the cone, indicating that the resultant shear contact force is perpendicular to the penetration direction and no longer contributes to the penetration resistance.

3.4 Statistical summary and visualization of the contact forces

A clearer picture of the individual interface contact forces at a certain penetration depth can be obtained by examining the statistical polar plot (Fig. 8) and the visualized force chain network (Fig. 9).

The polar bars become shorter (Fig. 8) with the increase of the rotational velocity, indicating the decrease of the contact numbers. Meanwhile, the force chains become weaker and more sparse (Fig. 9). The polar bars spread to a wider range and shift to higher contact angles in general (Fig. 8), indicating an increase in the average contact angle. The average contact angle changes from 47.32 to 58.93°, which is close to the contact angle of the resultant contact forces (Fig. 7b). The average contact force decreases with rotational velocity, except for the case for 400 rpm (2.99 N). The contact force changes from 2.55 N for the control case to 1.09 N for the 200 rpm case. In summary, the decreasing number of contacts, the smaller and more horizontal contact forces all contribute to the decrease of the penetration force.

Figure 9 also shows that with increasing rotational velocity, the distribution of the strong contact forces (the forces that are larger than the average contact normal force [42, 63]) within the soil sample becomes more localized. This indicates that the soil stress state at a location farther

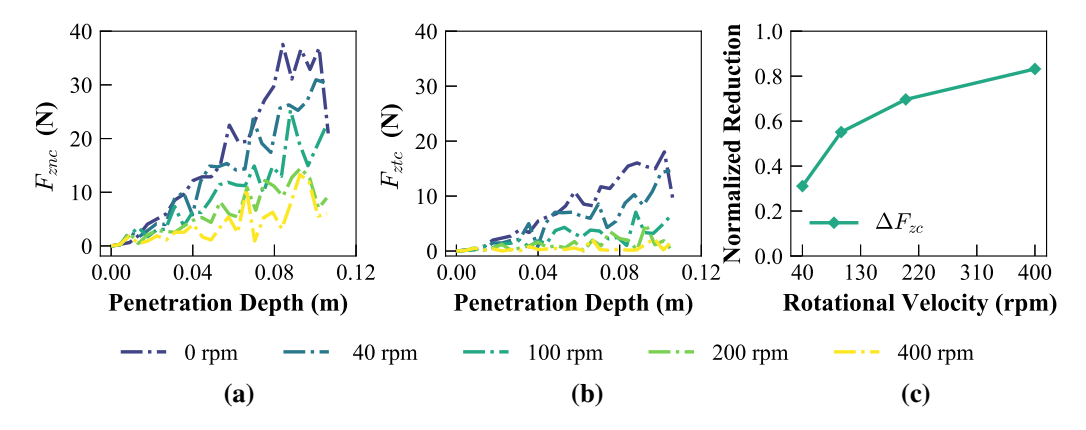


Fig. 6 Cone penetration force components and the relative reductions under different rotational velocities: **a** vertical component of the contact normal force on the cone (F_{zrc}); **b** vertical component of the contact shear force on the cone (F_{zrc}); **c** relative reduction of cone penetration force (Force differences were calculated between the rotational cases (40 rpm, 100 rpm, 200 rpm, and 400 rpm) and the control case (0 rpm) when the penetration depth is from 0.06 to 0.09 m; the relative reduction was calculated by normalizing the force difference with the cone penetration force in the control case)



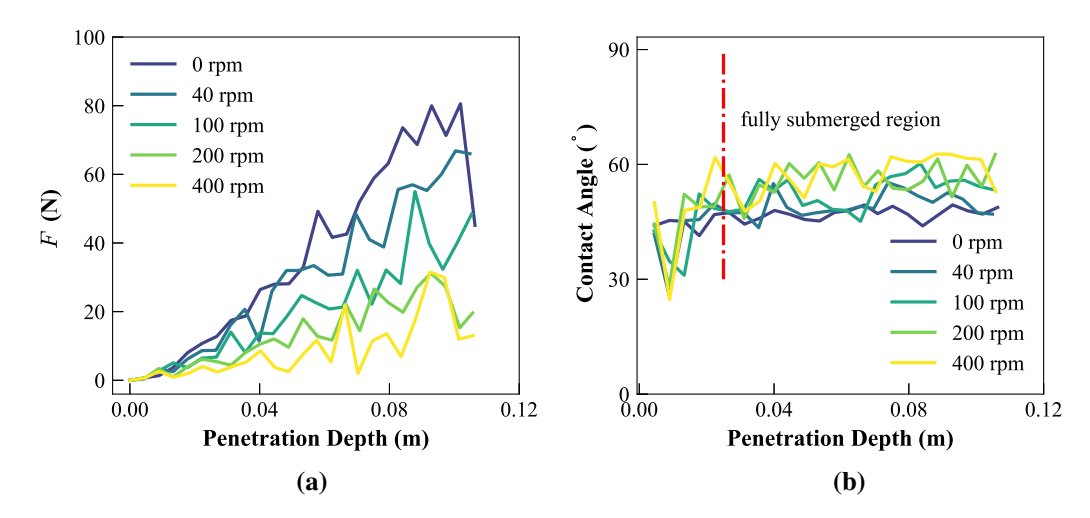


Fig. 7 Resultant contact force (F) and contact angle on the cone (θ) : a resultant contact force; b contact angle (the angle between the resultant contact force and the total cone penetration force; the dash-dot line marks the start of the full submerge of the cone)

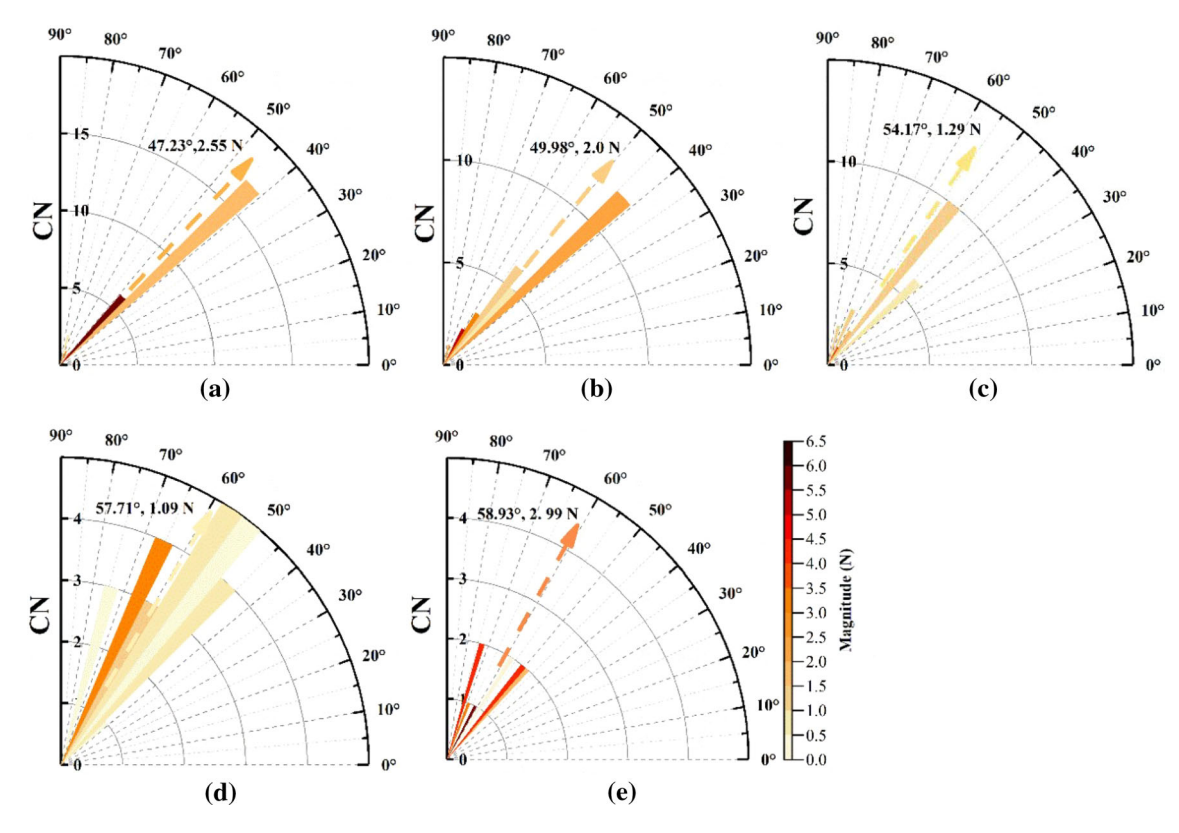


Fig. 8 Distribution of contact force and contact angle on the cone under different rotational velocities: **a** 0 rpm; **b** 40 rpm; **c** 100 rpm; **d** 200 rpm; **e** 400 rpm. (The color represents the magnitude of the resultant contact force; the dashed arrows indicate the average contact angles; the color of the dashed arrow represents the magnitude of the average contact force; penetration depth = 0.097 m)

from the cone is less affected for the fast-rotating cases and, thus, the increasing rate of penetration resistance (slope of curves in Fig. 3a) decreases with rotational velocity.

3.5 Particle trajectory and displacements

Changes in contact forces are associated with the trajectory and displacement of particles. Trajectories of 53 particles in the measurement sphere are analyzed (Fig. 22 in the "Appendix"). Only the trajectories for a single select



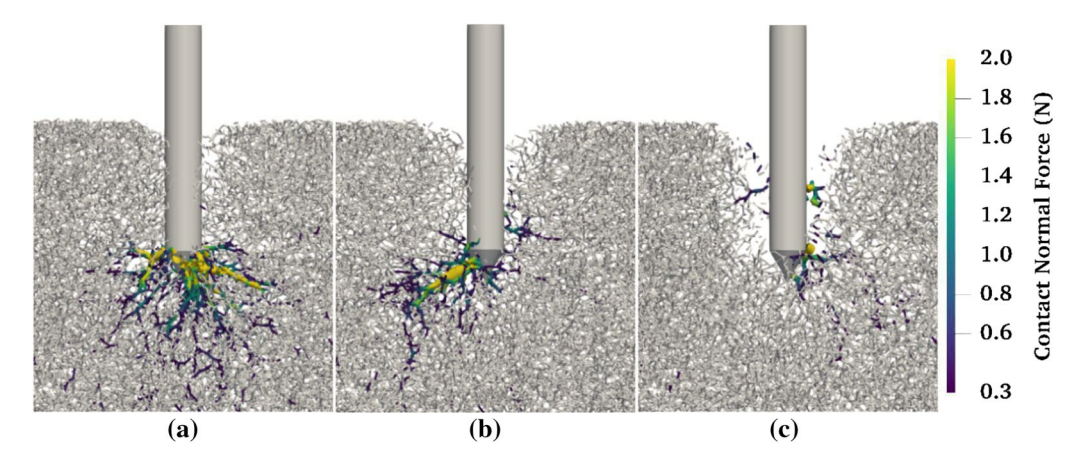


Fig. 9 Force chain network at the final stage under different rotational velocities: a 0 rpm (control case); b 100 rpm; c 400 rpm. The color indicates the magnitude of the contact normal force; contact normal forces smaller than the average value (0.3 N) are represented using gray color; the white spaces indicate there are no contact normal forces

particle, which was initially located along the centerline of the penetrator, are provided in Fig. 10 to illustrate the general trends. Figure 10 reveals distinct differences between the spatial trajectories of the particle in the control case and those in the 400 rpm case. While the particle moves downward and sideways in the control case, it is forced to move along a spiral path in the 400 rpm case.

The trajectories can be divided into three stages based on the relative vertical positions between the cone tip and the monitoring particle. In Stage I, the cone tip is above the monitoring particle; in Stage II, the particle is above the cone tip but below the cone shoulder; and Stage III occurs after the cone shoulder has passes the monitoring particle. In Stage I, the particles move slightly downward and sideways in both the control case and the case at 400 rpm; this finding is attributed to the compression effect from the early penetration. In Stage II, the particle in the control case mainly moves sideways, following more or less the same radial direction as in Stage I; the particle in the 400 rpm case starts to rotate around the cone as it is pushed downward and sideways; at the end of Stage II, the particle in both cases is pushed to a radial distance that is approximately the radius of the cone shoulder. In Stage III, the particle in the control case moves mainly downward along the shaft while the particle in the 400 rpm case continues to spiral around the shaft. After Stage I, the particle in the 400 rpm case completes about 1.5 rounds of rotation, while the penetrator itself completes about 16 rounds; the particle also travels much deeper than that in the control case.

The particle displacement field around the cone and shaft were also analyzed (Figs. 20 and 21 in the "Appendix"). In general, penetration without rotation pushes the particles around the centerline of the penetrator downward and sideways; pure rotation causes particles close to the

penetrator to rotate; the particle displacement fields caused by rotational penetration appear as the combination of those by vertical penetration and pure rotation.

4 Discussions

Previous studies attribute the rotation-induced reduction of penetration force to either the breakage of force chains [30] or the rotation of the contact shear forces [7, 47]; although empirical or analytical correlations between penetration resistance and the relative slip velocity (the ratio between rotational and translational velocities) have been proposed, the involved assumptions were often too strong and did not reflect the fundamental mechanisms. In this section, the findings from this study are used to validate or challenge the assumptions used in previous studies and to provide insights on the design of self-burrowing robots.

4.1 Testing the "force chain breakage" hypothesis

Jung et al. [30] proposed that the reduction in penetration force on a rotary conical intruder is solely due to the breaking of the force chains around the cone. The current study provides direct particle-level evidence to support the breakage of the force chains near the cone, as shown in Fig. 9, and the reduction of the contact numbers as shown in Figs. 5 and 8.

In Jung et al. [30], it was also postulated that since the rotational velocity (or slip velocity v_s) on the cone surface depends on the angular velocity (ω) and the radial distance from the cone centerline (r): ($v_s = \omega r$), the force chain breakage will be more effective in the outer region (near the cone shoulder) than the inner (near the cone tip).



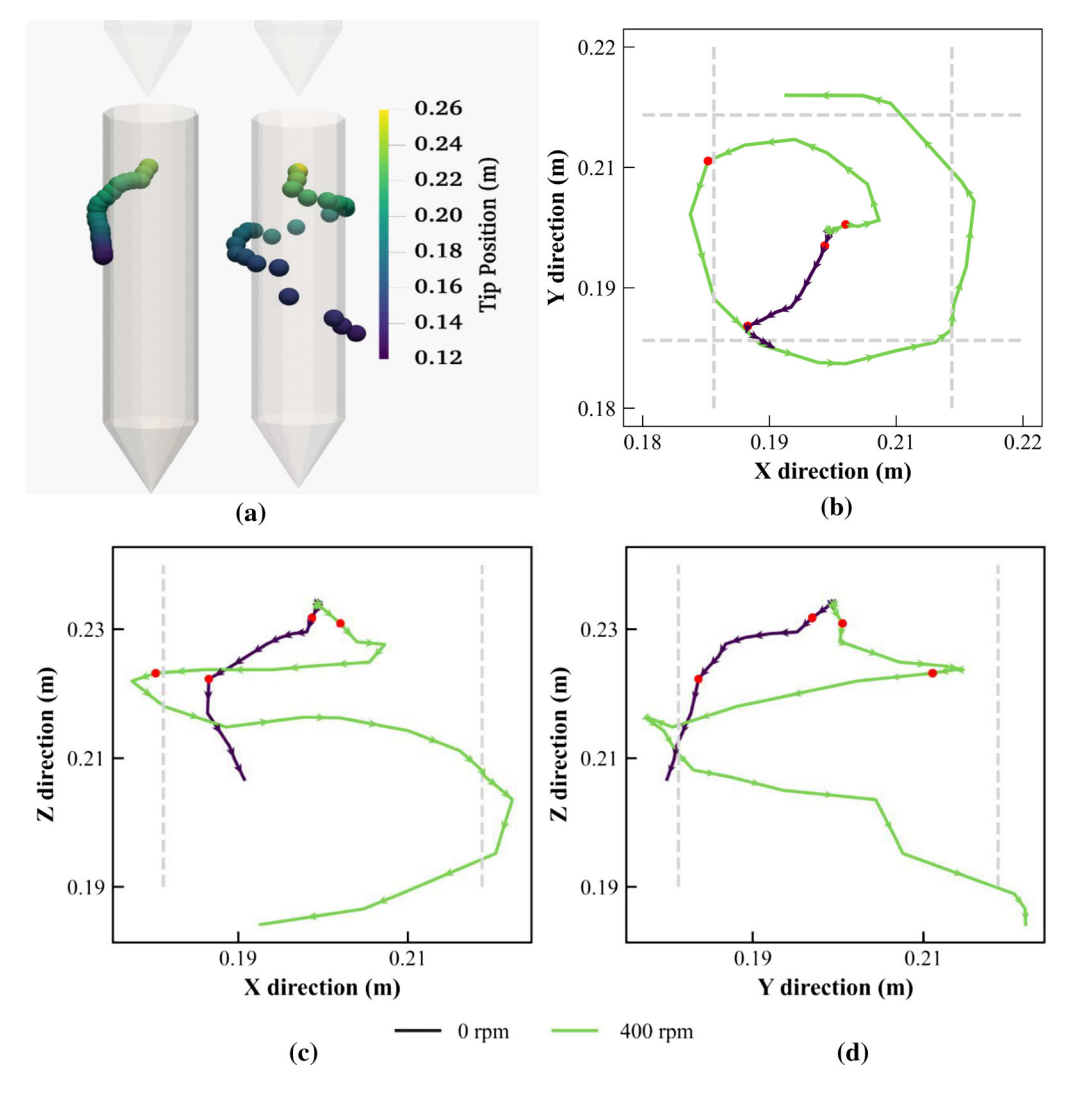


Fig. 10 Particle trajectories of select particles in the measurement sphere for the control case and the 400 rpm case shown in: \bf{a} the 3D space; \bf{b} the xy plane; \bf{c} the xz plane; and \bf{d} the yz plane. In \bf{a} , the colored spheres indicate the evolution of the position of the same select particle but at different time instants; the starting and end time instants were indicated by the locations of the penetrator. In $\bf{b-d}$, the arrows indicate the traveling directions of the particles; the red points mark the change of stages; and the dashed lines indicate the coordinate bounds of the penetrator

Figure 11 visualizes the particles in contact with the cone at a penetration depth of 0.11 m for the control, 100 rpm, and 400 rpm cases. To obtain the distribution of the number of contacts on the cone, the cone surface was divided into four regions with equal height as shown; the number of particles per unit cone surface area is shown in Fig. 11d. The results confirm that the contact force chain breaks more effectively with a higher slip velocity, which can result from increased rotational angular velocity and/or the radial distance from the cone centerline.

The particle-scale data provided direct evidence to support the force chain breakage theory. However, the explanations provided in Jung et al. [30] overlooked the contributions from the changes in both the magnitude and

the direction of the individual contact forces (Fig. 8), which are discussed below.

4.2 Challenging the common assumptions in developing analytical models

Analytical expressions of rotational penetration resistance were presented in Bengough et al. [7] and Sherif et al. [47]. Despite differences in the terminologies and notations, both expressions are equivalent, and they were derived based on the same assumptions. For simplicity, only the expression in Bengough et al. [7] is presented here (Eq. 5).



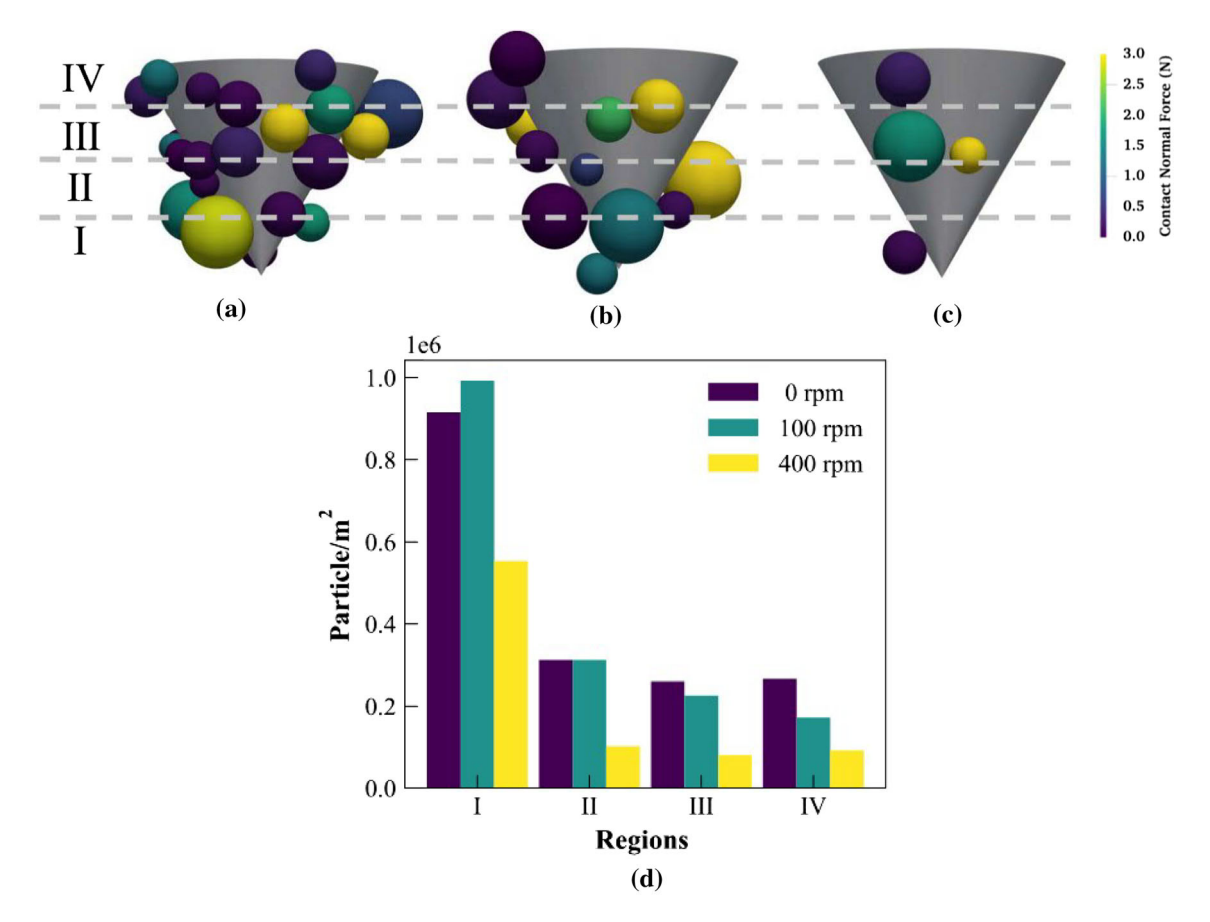


Fig. 11 Cone-particle contacts: **a** 0 rpm; **b** 100 rpm; **c** 400 rpm (in this subfigure, the color represents the magnitude of the contact normal force, the size of the particle is proportional to its diameter, the penetration depth is 0.11 m, the dashed lines divide the height of the cone into four regions); **d** number of particles per unit cone surface area. (Note that the scale of the vertical axis is 10⁶)

$$\begin{split} q_{\text{cRot}} &= \sigma + \frac{(\sigma \tan \delta + c_{\text{a}}) T_{\text{p}}^2 v_{\text{p}}^2}{2 \pi^2 R^2 \sin \alpha} \\ &\times \left[\left(\sec^2 \alpha + \frac{4 \pi^2 R^2}{T_{\text{p}}^2 v_{\text{p}}^2} \right)^{1/2} - \sec \alpha \right] \end{split} \tag{5}$$

where q_{cRot} is the rotational penetration resistance; σ is the stress normal to the cone surface; δ is the soil–penetrator friction angle; c_{a} is the soil–penetrator adhesion (the adhesion is zero for Ottawa sand F65); R and α are the radius and semi-angle of the cone, respectively; and v_{p} and T_{p} are the vertical penetration velocity and the rotational period, respectively.

The detailed derivation for Eq. (5) can be found in [7], in which three major assumptions were made: (1) the soil properties are homogenous at the scale of the cone; (2) the soil is in continuous contact with and slides along the cone surface; and (3) the normal contact stress does not change during rotation. Another implicit assumption is that the soil body does not move in relative to the cone, so that the rotation of the shear stress on the cone surface can be related to the rotational speed (Fig. 12a and Eq. 6).

$$\cos\theta = \frac{v_{\rm p}T_{\rm p}}{\sqrt{v_{\rm p}^2T_{\rm p}^2 + 4\pi^2r^2\cos_{\alpha}^2}} = \frac{v_{\rm p}\frac{60}{\rm rpm}}{\sqrt{v_{\rm p}^2\left(\frac{60}{\rm rpm}\right)^2 + 4\pi^2r^2\cos_{\alpha}^2}}$$
(6)

The findings in this study, however, challenge all these assumptions. As shown in Fig. 9, the distribution of the contact forces around the cone is not homogenous; the trajectory of the monitor particle in Fig. 10 shows that the soil is not in continuous contact with the cone surface and in fact, the forming and breaking of particle-penetrator contacts are dynamic and complex. The rotation of the contact shear force vector can also be directly calculated as the angle between the particle-penetrator contact shear force vector and the vector pointing from the tip to the contact itself (Fig. 12a). The comparison between the analytical and numerical results for two rotational cases is shown in Fig. 12b. The analytical results show that the rotation of the contact shear force increases with the rotational speed and the radial distance from the contact to the cone centerline (r); with a rotational speed of 400 rpm, the rotation of the contact shear force vector approaches 90°



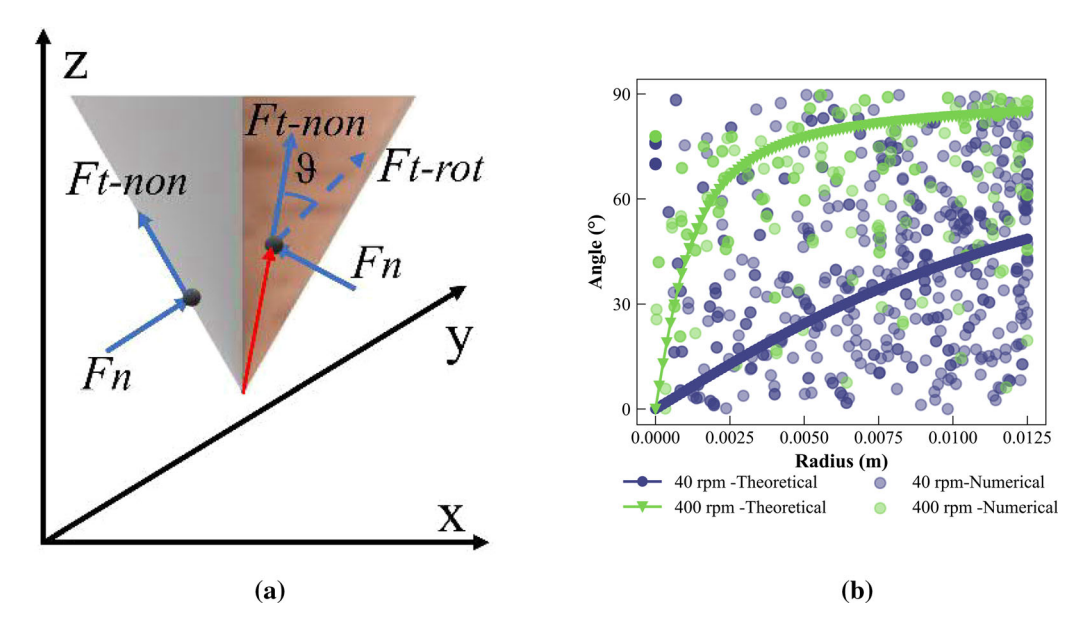


Fig. 12 a Illustration of rotation of the contact shear force vector due to rotation. The left and right halves of the cone represent a non-rotational and a rotational case, respectively. The non-rotational contact shear force aligns with the vector connecting the cone tip and the contact point. The angle ϑ denotes the change of the direction of the contact shear force; **b** the angle ϑ , which is calculated using Eq. (6) and the results from the numerical simulation

near the cone shoulder, indicating negligible contribution to the vertical penetration resistance. However, the numerical data shows wide distributions of rotation angles although more data points are indeed located close to the analytical curves.

The strongest assumption in developing the analytical models is that the magnitude of the normal contact stress on the cone does not change due to rotation. From Fig. 6a, it is evident that the contact normal force, and thus the normal contact stress, decreases with increasing rotational speed. By assuming a constant normal contact stress, it seems to overestimate the rotational penetration resistance. This is indeed the case when comparing the normalized penetration resistance calculated using the analytical model (Eq. 5) and that directly obtained from the DEM simulations in this study (Fig. 13). Both models capture similar trends for the development of penetration resistance with depth without rotation and for the decrease in penetration resistance with increasing rotational speed; however, the analytical model predicts higher penetration resistance than the DEM model, and the overprediction is more significant for higher rotation speeds. The overprediction is mainly due to the assumption of constant normal stress on the cone.

4.3 Meso-scale interpretation: principal stress reduction and rotation

The analytical models discussed above were used as an attempt to correlate the penetration resistance with meso-

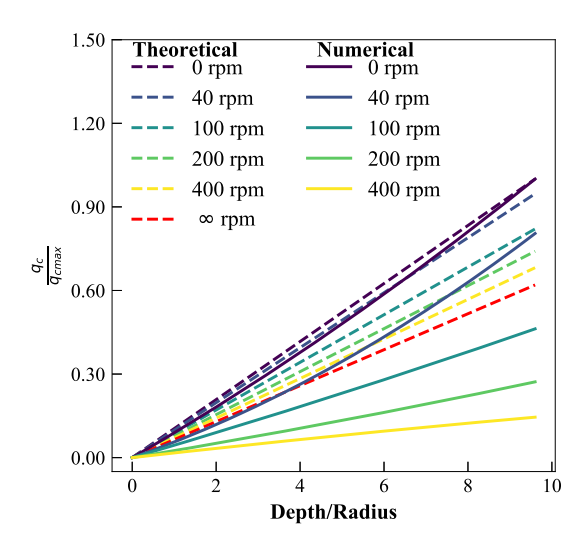


Fig. 13 Normalized cone penetration resistance vs. normalized penetration depth. The cone penetration resistance q_c is normalized by the resistance for the control case at the maximum depth of 0.11 m (q_{cmax}); the penetration depth is normalized by the radius of the penetrator. When the rotational velocity approaches ∞ , the rotational penetration resistance approaches σ in Eq. 5)

scale stress terms, but they neglected the changes in the magnitude of the stress. Here, the numerically obtained contact force data in a measurement box (Fig. 1b) is homogenized, and the principal stresses are computed and analyzed. Since the particles in contact with the penetrator also interact with the surrounding particles, meso-scale analysis can provide a perspective on how the soil mass collectively responds to rotational penetration and how the



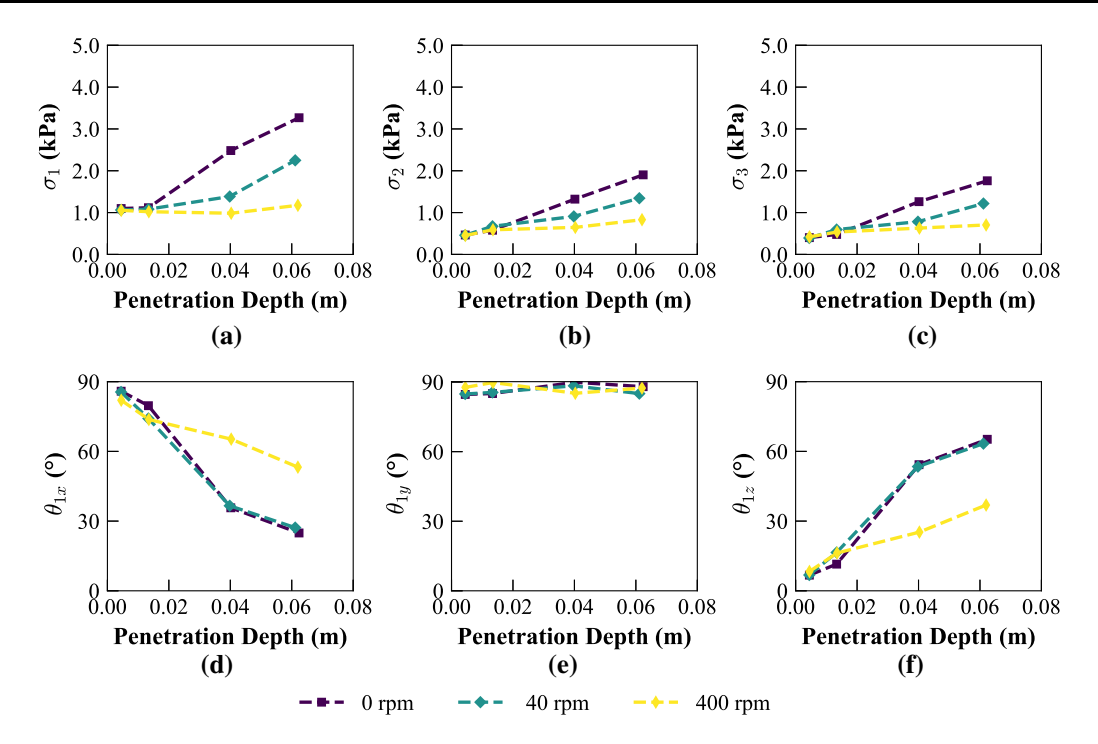


Fig. 14 Evolution of the magnitude of the principal stresses: a major; b intermediate; c minor; and angle between the major principal stress and d the negative x direction; e positive y direction and f positive z direction. (The coordination system follows the right-hand rule as shown in Fig. 12a)

reduction in penetration resistance can be interpreted using stress terms. It also highlights the needs to consider the rotation-induced reduction on normal stress on the cone when developing continuum-based analytical models.

Figure 14a–c show the evolution of the magnitude of the principal stresses during rotational penetration up to the point where the tip of the cone approaches the bottom of the measurement box. All the three principal stresses increase with penetration depth but decrease with the rotational velocity; the reduction of the major principal stress is more significant than that of the intermediate principal stress and minor principal stress.

The principal stresses also rotate due to the penetration and rotation of the rod. The change of the orientation of the major principal stress is shown in Fig. 14d-f. θ_{1x} , θ_{1y} and θ_{17} represent the angle between the major principal stress and the x, y, and z direction, respectively (See Fig. 12a for the coordination system). Before penetration, θ_{1x} , θ_{1y} and θ_{1z} are 90°, 90°, and 0°, respectively, indicating that the major principal stress is in the z direction and the soil is in the at-rest state. As the cone tip approaches the measurement box, θ_{1y} keeps around 90° (Fig. 13e), indicating that the major principal stress is always perpendicular to the y direction and that the shear stress induced by the rotation (along the y direction) is relatively small comparing to that induced by the penetration (along z direction). Meanwhile, θ_{1x} decreases and θ_{1z} increases with the penetration depth, and the two angles are complementary angles in the xz plane. Furthermore, the major principal stress inclines more towards the z direction and away from the x direction as the rotation speed increases, due to rotation-induced reduction of the magnitude of the stresses.

Figure 15 presents the direction and magnitude of the major principal stress at the final penetration depth on the xz plane. It shows that a higher rotational velocity results in reduced magnitude of the major principal stresses as well as reduced angles with respect to the positive z axis. The

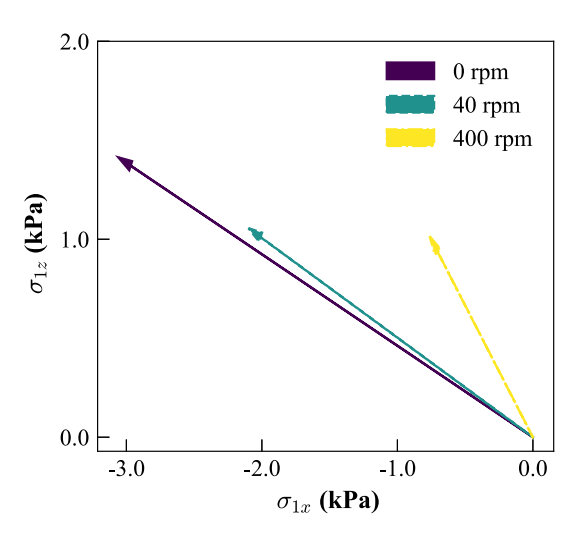


Fig. 15 The rotation and shrinkage of the major principal stress vectors in the xz plane with increasing rotational velocity. The data plotted in this figure corresponds to the maximum penetration depth



overall effect is that the vertical component of the major principal stress is reduced.

4.4 Absolute rotational velocity vs. relative slip velocity

Previous studies indicate that the reduction in the cone penetration force does not solely rely on the absolute value of the rotational velocities; it is commonly held that the relative slip velocity or pitch $\left(u = \frac{\nu_s}{\nu_p} = \frac{\omega r}{\nu_p}\right)$ dictates the effectiveness of reduction [16, 30, 47]. To further validate this argument, a second series of simulations were conducted in which the relative slip velocities were kept as the same as the original series but with reduced vertical penetration velocity (0.01 m/s) and adjusted rotational speeds (0, 10, 25, 50, and 100 rpm). The results confirmed that it is the relative slip velocity rather than the rotational velocity itself that controls the effectiveness of reduction (Fig. 16).

4.5 Implications to self-burrowing robot design: low penetration force and low power requirement

The above analysis validates that rotation causes significant disturbance to the surrounding soil, contributing to the reduction of penetration resistance. The importance of a lower penetration resistance for an autonomous penetrator is underscored by the recent unsatisfactory performance of NASA's Heat Flow and Physical Properties Package (HP³) probe, which was not able to penetrate the Martian ground as planned [23]. If the design purpose is just to enable the robot to burrow into the soil as easily as possible, a higher rotational velocity and thus a lower penetration force would be preferred. However, force is not always the only

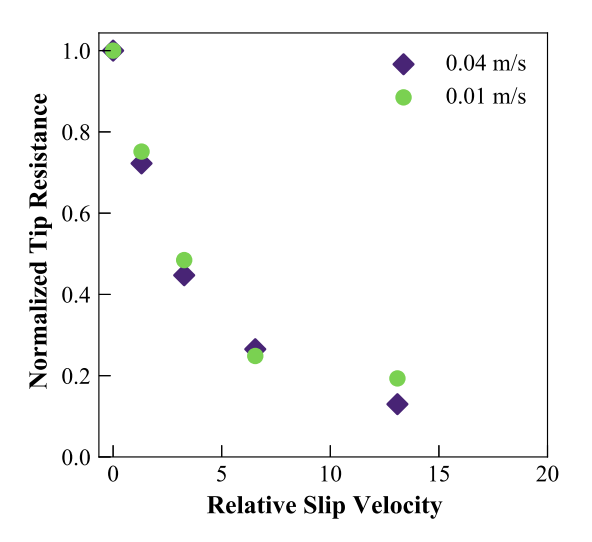


Fig. 16 Normalized cone penetration resistance under different relative slip velocities

design criterion. When considering the energy efficiency of a robot, power consumption (Eq. 4) can be used as a metric for optimization.

Figure 17 presents the average power consumption of the penetrators during the entire penetration process (0-0.11 m). The power consumption first decreases and then increases with the increasing rotational speed. The power consumption of the non-rotational penetrator case is about 25.68 W, while that of the penetrator with a rotational speed of 200 rpm is 17.67 W, which is equivalent to a 30% reduction. At an even higher rotational speed, the power consumption increases again. The general trend can be explained by Eq. (4), which shows that the power consumption depends not only on the magnitude of force and torque, but also the vertical velocity and rotational speed. One can notice the sharp increase of the torque on the shaft at a depth of 0.09 m for the 400 rpm case (Fig. 4b). This sharp increase is most probably an outlier due to the discrete nature of the soil. At depths below 0.09 m, the torque level quickly reverted to a much lower level and continued the previous trend as if the outlier was not present. However, even if the outlier is removed, the power consumption of the 400 rpm case was still much higher than the 200 rpm case. This confirmed that the power increase in the 400 rpm case is mainly due to the much higher rotational speed (term ω in Eq. 4) instead of the sharp increase in torque at a random depth.

This analysis indicates that there may exist an optimal rotational speed to minimize the power consumption. Figure 17 also shows that from 0 to 200 rpm, the reduction of the total power is caused by the reduction in the contribution of the cone (the lower part of the bars in Fig. 17), since the power consumed on the shaft (the upper part of the bars) increases with the speed of rotation. These results imply that rotating only the tip may further reduce the

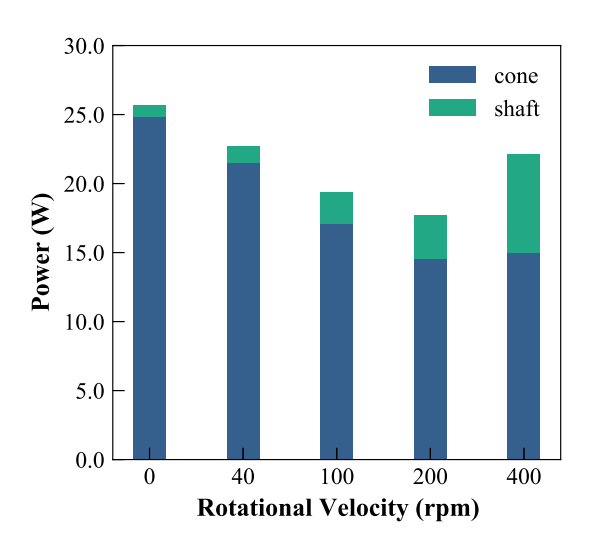
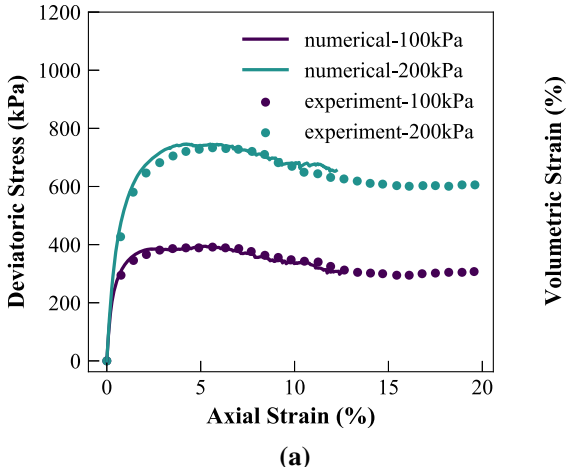


Fig. 17 Power consumption under different rotational velocities





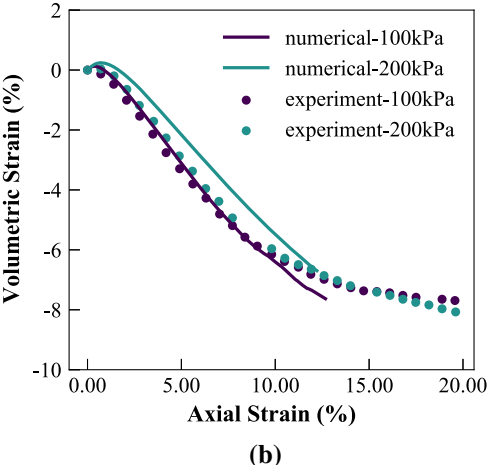


Fig. 18 Calibration and validation of parameters using triaxial test of Ottawa F65: a deviatoric stress–axial strain curve; b volumetric strain–axial strain curve

energy consumption but can still be effective in reducing the penetration force. Inspired by the self-burial of seedawns and the findings from this study, a prototype horizontal self-burrowing robot has been developed and tested in the authors' group; the preliminary results can be found in Huang and Tao [25].

5 Conclusions

In this study, rotational penetration in shallow dry sand was investigated using DEM simulations. With the rich multiscale data obtained in this study, the fundamental mechanisms on penetration force reduction were investigated, and existing hypotheses were tested. The findings of the research also shed light on the design of self-burrowing robots.

The numerical simulation results confirm that the cone penetration force decreases with the increase in the rotational velocity, or more rigorously, the relative slip velocity. The rotation-induced reduction in the cone penetration force is attributed to combined effects of reduced particle—penetrator contact number, reduced contact forces, and increased inclination of the contact forces with increasing relative slip velocity.

The results from this study validated the existing "force chain breakage" hypothesis: the force chain network around the cone becomes weaker and more sparse with the increase in rotational velocity; in addition, the force chain breakage is more effective at the cone shoulder region than the tip region. The results also challenged the commonly adopted assumptions in developing the analytical models for rotational penetration. It is demonstrated that the contact forces are neither homogeneous nor continuous; the normal stress is not a constant value but decreases with the

increase of rotational velocity; the rotation of the contact shear force vector does not follow the simple trigonometry based on the penetration and rotational velocities. Future improvements on the analytical models may include the rotation-induced reduction and inclination of the contact forces on the cone.

The findings from this study also suggest that incorporating rotation in a self-burrowing robot may reduce not only the burrowing forces but also the overall power requirement.

6 Appendix

6.1 Moment transfer law

The computational costs can be kept at a lower level even for a large number of particles by using the regular spherical shape for the particles. Rolling resistance can be included to consider the granular geometry or rough surface texture of the soil particles [6, 44, 61]. An elastic contact moment (M_e) is introduced to account for the rolling effect between two contacting spherical particles. The elastic contact moment can be expressed as,

$$M_{\rm e} = k_{\rm r}\theta_{\rm r}$$

where $k_{\rm r}$ and $\theta_{\rm r}$ are the rolling stiffness coefficient and the rotation angle between two contacting particles.

The rolling stiffness is a function of tangential contact stiffness (k_s) and a dimensionless coefficient (β).

$$k_{\rm r} = \beta \cdot k_{\rm s} \cdot r_{\rm a} \cdot r_{\rm b}$$

where r_a and r_b are the radii for the two contacting particles.



The elastic contact moment, and thus the rolling resistance, can be limited by the introduction of a plastic moment (M_p) as

$$M_{\mathrm{p}} = \eta \left(\frac{r_{\mathrm{a}} + r_{\mathrm{b}}}{2} \right) \cdot \parallel F_{\mathrm{n}} \parallel$$

where η is a dimensionless coefficient used for the plastic moment; $||F_n||$ is the normal value of the normal contact force.

Therefore, the rolling moment can be represented as, $M_{\rm r}=\min(M_{\rm e},M_{\scriptscriptstyle
m D})$

6.2 Justification of the selected model geometry parameters

Theoretically, the parameters used in the numerical model should be set as close to the field condition as possible to achieve maximum accuracy. However, if realistic sizes of the particles, penetrator, and chamber are to be simulated, hundreds of billions of particles should be prepared, which is far beyond the capability of our computational resources. Butlanska [9] found that there is no significant effect on the macroscale properties of the sand if the particle size is scaled up by 50 times in DEM. Butlanska et al. [10] and Arroyo et al. [4] found that a higher ratio n_p results in smoother penetration resistance curves. Khosravi et al. [33] reported that the typical n_p values used in previous 3D DEM modeling studies were in the range of 2–25, with the most commonly adopted value being around 3.

The diameter of the measurement sphere is 0.025 m, which is the same as the diameter of the penetrator. The length of the measurement cubic box is 0.075 m. The average diameter of the soil particle is 0.005 m. The purpose of the measurement sphere was to record the trajectories of the 53 circumscribed particles during the

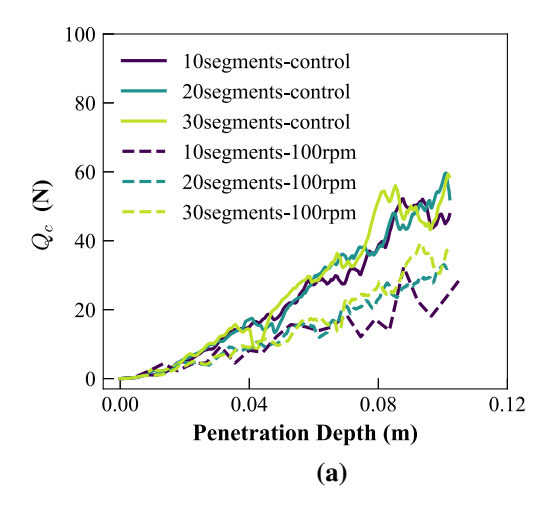
penetration process. The ratio between the length of the measurement box and the average diameter of the granular particle is $D/D_{50}=15$. There are around 4000 particles inside the measurement box. The authors reviewed the selection of measurement circle/sphere sizes adopted in existing DEM studies (Table 2) and found that D/D_{50} varied within a broad range. Both the ratios for the measurement sphere and for the measurement box in this study are within this range.

6.3 Calibration and validation of the particlelevel parameters

Triaxial compression tests of Ottawa F65 dry sand with confining pressure levels of 100 kPa and 200 kPa [5, 58] are used as the reference of calibration and the reference for validation, respectively. The numerical triaxial data match well with the experimental results based on the peak strength and stiffness (Fig. 18). The slight discrepancy in the volumetric strain curves in the validation set indicates that using the calibrated parameters may result in a slightly smaller dilation angle than the experimental results.

6.4 Effect of the cross section geometry of the penetrator on resistive force

The resistive force for the control case and the 100 rpm case with penetrators approximated using different number of segments is shown in Fig. 19. The cone penetration force increases slightly with the increase of the segments, while the shaft resistive force does not show any clear trend.



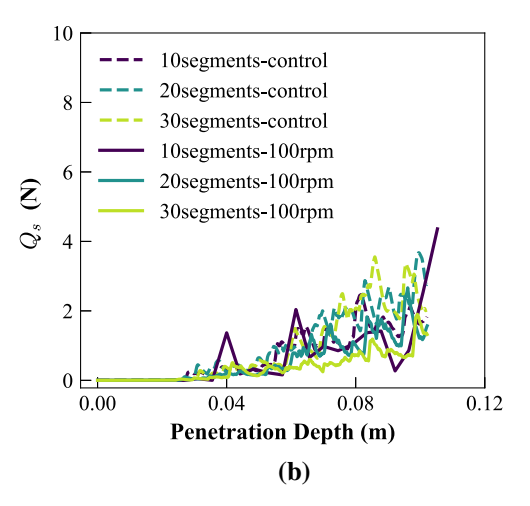


Fig. 19 Resistive force for the control case and 100 rpm case with different segments: a cone penetration force; b shaft resistive force



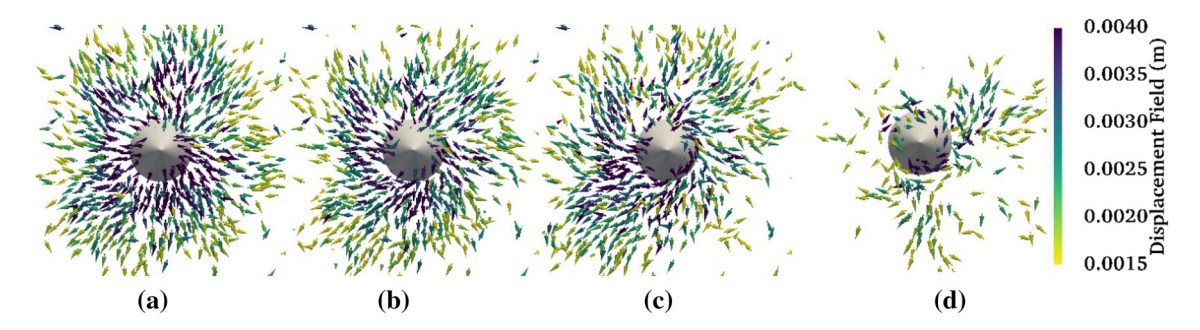


Fig. 20 Bottom view of particle displacement field around the cone under different rotational velocities: **a** 0 rpm; **b** 100 rpm; **c** 400 rpm; **d** pure rotation at 400 rpm (the color represents the magnitude of the displacement)

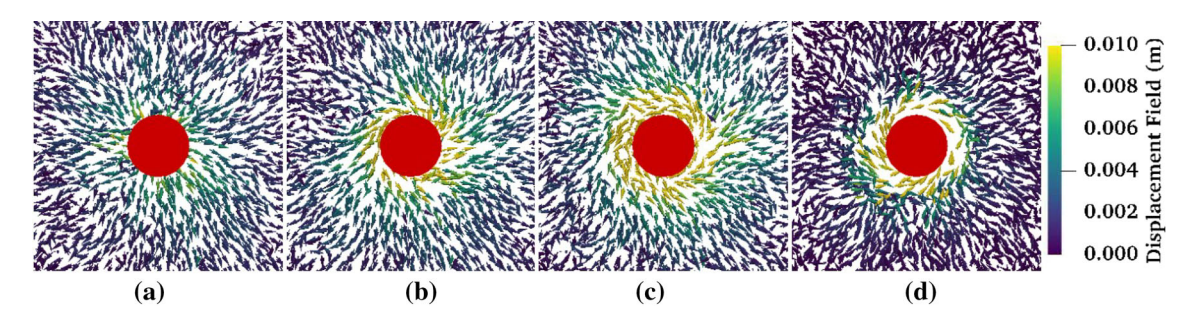


Fig. 21 Top view of particle displacement field around the shaft under different rotational velocities: **a** 0 rpm; **b** 100 rpm; **c** 400 rpm; **d** pure rotation at 400 rpm (the color represents the magnitude of the displacement)

6.5 Particle displacement field around the shaft under different rotational velocities

A bottom view of the particle displacement field around the cone (at the final penetration depth of 0.11 m) under different rotational velocities is shown in Fig. 20, which also includes that of a pure rotational case (with zero vertical velocity) for comparison. Without rotation (Fig. 20a), the cone pushes the particles sideways; with pure rotation (Fig. 20d), the particles close to the cone rotate, and those far from the cone are pushed sideways. The displacement field of the rotational penetration cases (Fig. 20b, c) appears to be a combination of the displacement field of the control case and that of the pure rotation case; the rotational particle movement are more pronounced for the case with faster rotation. A top view of the particle displacement field around the shaft, which presents similar trends, was also included in the "Appendix" (Fig. 21) completeness.

A top view of the particle displacement field around the shaft under different rotational velocities is shown in Fig. 21. The particle displacement patterns are similar to those around the cone Fig. 20. The particles travel sideways without rotation (Fig. 21a), while the particles rotate around the shaft with the rotational movement (Fig. 21b–d). The particles adjacent to the shaft rotate, but those far away from the shaft are pushed sideways for the case with

pure rotation (Fig. 21d). With both rotation and penetration, the displacement of the particles close to the shaft present a combination of rotational and sideways translational movements. The coherent rotational movements of the particles around the shaft are much clearer than those around the cone due to the uniform cross section of the shaft.

6.6 The trajectories of particles in the measurement sphere

The trajectories of the particles in the measurement sphere are shown in Fig. 22. The trends are found to be consistent: the particles for the control case mainly travel sideways and downward (Fig. 22a), while the particles for the 400 rpm case move along spiral paths (Fig. 22b).

Acknowledgements This material is based upon work supported by the National Science Foundation (NSF) under NSF CMMI 1849674 and CMMI 1841574. Any opinions, findings, and conclusions or recommendations expressed in this material are those of the authors and do not necessarily reflect those of the NSF. We also would like to thank the anonymous reviewers whose constructive comments helped us improve the overall quality of the paper.



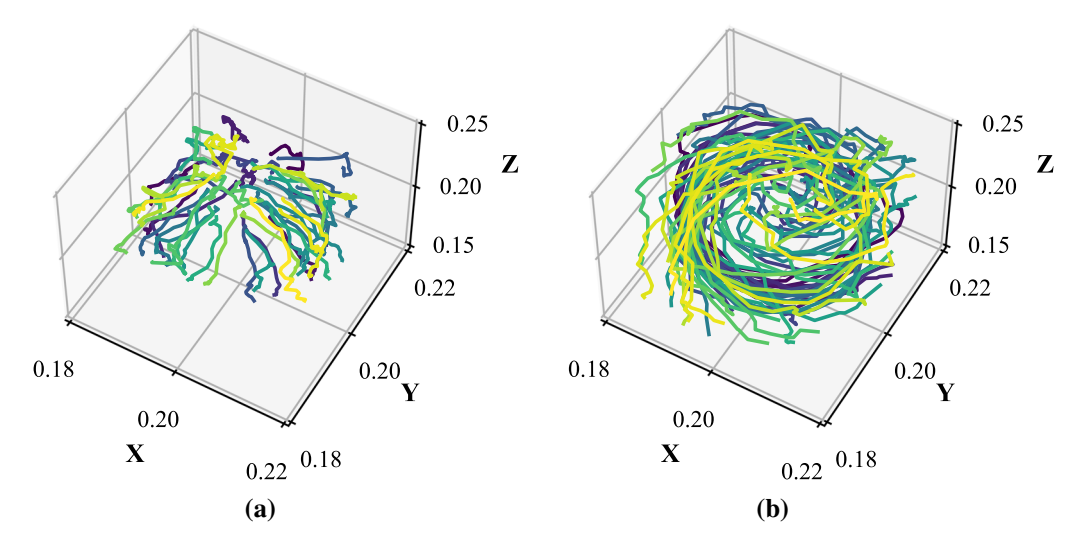


Fig. 22 Trajectories of all the 53 particles in measurement sphere: a trajectories of particles for the control case; b trajectories of particles for the 400 rpm case (Color is used to differentiate particles)

References

- Abraham Y, Elbaum R (2013) Hygroscopic movements in Geraniaceae: the structural variations that are responsible for coiling or bending. New Phytol 199:584–594. https://doi.org/10. 1111/nph.12254
- Abraham Y, Tamburu C, Klein E, Dunlop JWC, Fratzl P, Raviv U, Elbaum R (2012) Tilted cellulose arrangement as a novel mechanism for hygroscopic coiling in the stork's bill awn. J R Soc Interface 9:640–647. https://doi.org/10.1098/rsif.2011.0395
- Ansell AD, Trueman ER (1967) Burrowing in Mercenaria Mercenaria (L.) (Bivalvia, Veneridae). J Exp Biol 46:105–115. https://doi.org/10.1242/jeb.46.1.105
- Arroyo M, Butlanska J, Gens A, Calvetti F, Jamiolkowski M (2011) Cone penetration tests in a virtual calibration chamber. Geotechnique 61:525–531. https://doi.org/10.1680/geot.9.P.067
- Badanagki M (2020) Centrifuge modeling of dense granular columns in layered liquefiable soils with varying stratigraphy and overlying structures. In: PhD thesis, University of Colorado at Boulder
- Belheine N, Plassiard J-P, Donzé F-V, Darve F, Seridi A (2009) Numerical simulation of drained triaxial test using 3D discrete element modeling. Comput Geotech 36:320–331. https://doi.org/ 10.1016/j.compgeo.2008.02.003
- Bengough AG, Mullins CE, Wilson G (1997) Estimating soil frictional resistance to metal probes and its relevance to the penetration of soil by roots. Eur J Soil Sci 48:603–612. https:// doi.org/10.1111/j.1365-2389.1997.tb00560.x
- Borela R, Frost JD, Viggiani G, Anselmucci F (2021) Earthworm-inspired robotic locomotion in sand: an experimental study with X-ray tomography. Géotechnique Lett 11:66–73. https://doi.org/10.1680/jgele.20.00085
- 9. Butlanska J (2014) Cone penetration test in a virtual calibration chamber. In: TDX (Tesis Doctorals en Xarxa)
- Butlanska J, Arroyo M, Gens A (2010) Size effects on a virtual calibration chamber. In: Numerical methods in geotechnical engineering. CRC Press, Hoboken
- Chen Y, Khosravi A, Martinez A, DeJong J (2021) Modeling the self-penetration process of a bio-inspired probe in granular soils. Bioinspir Biomim 16:046012. https://doi.org/10.1088/1748-3190/ abf46e

- Chen RP, Tang LJ, Ling DS, Chen YM (2011) Face stability analysis of shallow shield tunnels in dry sandy ground using the discrete element method. Comput Geotech 38:187–195. https:// doi.org/10.1016/j.compgeo.2010.11.003
- Ciantia MO, O'Sullivan C, Jardine RJ (2019) Pile penetration in crushable soils: insights from micromechanical modelling. In: Proceedings of the XVII ECSMGE-2019 5247–5266. https://doi. org/10.32075/17ECSMGE-2019-1111
- Cui L, O'Sullivan C (2006) Exploring the macro- and micro-scale response of an idealised granular material in the direct shear apparatus. Geotechnique 56:455–468. https://doi.org/10.1680/ geot.56.7.455
- Darbois Texier B, Ibarra A, Melo F (2017) Helical locomotion in a granular medium. Phys Rev Lett 119:068003. https://doi.org/10. 1103/PhysRevLett.119.068003
- Deeks AD (2008) An investigation into the strength and stiffness of jacked piles in sand. PhD thesis, University of Cambridge
- Dorgan KM (2015) The biomechanics of burrowing and boring.
 J Exp Biol 218:176–183. https://doi.org/10.1242/jeb.086983
- Del Dottore E, Mondini A, Sadeghi A, Mattoli V, Mazzolai B (2017) An efficient soil penetration strategy for explorative robots inspired by plant root circumnutation movements. Bioinspir Biomim 13:015003. https://doi.org/10.1088/1748-3190/aa9998
- Elbaum R, Abraham Y (2014) Insights into the microstructures of hygroscopic movement in plant seed dispersal. Plant Sci 223:124–133. https://doi.org/10.1016/j.plantsci.2014.03.014
- Elbaum R, Gorb S, Fratzl P (2008) Structures in the cell wall that enable hygroscopic movement of wheat awns. J Struct Biol 164:101–107. https://doi.org/10.1016/j.jsb.2008.06.008
- Elbaum R, Zaltzman L, Burgert I, Fratzl P (2007) The role of wheat awns in the seed dispersal unit. Science 316:884–886. https://doi.org/10.1126/science.1140097
- Evangelista D, Hotton S, Dumais J (2011) The mechanics of explosive dispersal and self-burial in the seeds of the filaree, *Erodium cicutarium* (Geraniaceae). J Exp Biol 214:521–529. https://doi.org/10.1242/jeb.050567
- Greicius T (2020) NASA's mars InSight lander to push on top of the 'mole'. http://www.nasa.gov/feature/jpl/nasas-mars-insight-lander-to-push-on-top-of-the-mole
- 24. Gu M, Han J, Zhao M (2017) Three-dimensional discrete-element method analysis of stresses and deformations of a single geogrid-



- encased stone column. Int J Geomech 17:04017070. https://doi.org/10.1061/(ASCE)GM.1943-5622.0000952
- Huang S, Tao J (2022) Bioinspired horizontal self-burrowing robot. Charlotte, NC
- Huang S, Tao J (2020) Modeling clam-inspired burrowing in dry sand using cavity expansion theory and DEM. Acta Geotech 15:2305–2326. https://doi.org/10.1007/s11440-020-00918-8
- 27. Jerier J-F, Imbault D, Donze F-V, Doremus P (2009) A geometric algorithm based on tetrahedral meshes to generate a dense polydisperse sphere packing. Granul Matter 11:43–52. https://doi.org/10.1007/s10035-008-0116-0
- Jiang M, Dai Y, Cui L, Shen Z, Wang X (2014) Investigating mechanism of inclined CPT in granular ground using DEM. Granul Matter 16:785–796. https://doi.org/10.1007/s10035-014-0508-2
- Jing X-Y, Zhou W-H, Zhu H-X, Yin Z-Y, Li Y (2018) Analysis of soil-structural interface behavior using three-dimensional DEM simulations. Int J Numer Anal Meth Geomech 42:339–357. https://doi.org/10.1002/nag.2745
- Jung W, Choi SM, Kim W, Kim H-Y (2017) Reduction of granular drag inspired by self-burrowing rotary seeds. Phys Fluids 29:041702. https://doi.org/10.1063/1.4979998
- Jung W, Kim W, Kim H-Y (2014) Self-burial mechanics of hygroscopically responsive awns. Integr Comp Biol 54:1034–1042. https://doi.org/10.1093/icb/icu026
- 32. Kang C, Chan D (2018) Numerical simulation of 2D granular flow entrainment using DEM. Granul Matter 20:13. https://doi.org/10.1007/s10035-017-0782-x
- Khosravi A, Martinez A, DeJong JT (2020) Discrete element model (DEM) simulations of cone penetration test (CPT) measurements and soil classification. Can Geotech J 57:1369–1387. https://doi.org/10.1139/cgj-2019-0512
- 34. Li L, Wu W, Hesham El Naggar M, Mei G, Liang R (2019) DEM analysis of the sand plug behavior during the installation process of open-ended pile. Comput Geotech 109:23–33. https://doi.org/10.1016/j.compgeo.2019.01.014
- Lu Y, Frost D (2010) Three-dimensional DEM modeling of triaxial compression of sands. In: Soil behavior and geo-micromechanics. American Society of Civil Engineers, Shanghai, China, pp 220–226
- Ma Y, Evans TM, Cortes DD (2020) 2D DEM analysis of the interactions between bio-inspired geo-probe and soil during inflation-deflation cycles. Granul Matter 22:11. https://doi.org/ 10.1007/s10035-019-0974-7
- Maladen RD, Ding Y, Li C, Goldman DI (2009) Undulatory swimming in sand: subsurface locomotion of the Sandfish lizard. Science 325:314–318
- Maladen RD, Ding Y, Umbanhowar PB, Kamor A, Goldman DI (2011) Mechanical models of sandfish locomotion reveal principles of high performance subsurface sand-swimming. J R Soc Interface. https://doi.org/10.1098/rsif.2010.0678
- 39. Martinez A, Dejong J, Akin I, Aleali A, Arson C, Atkinson J, Bandini P, Baser T, Borela R, Boulanger R, Burrall M, Chen Y, Collins C, Cortes D, Dai S, Dejong T, Del Dottore E, Dorgan K, Fragaszy R, Frost JD, Full R, Ghayoomi M, Goldman DI, Gravish N, Guzman IL, Hambleton J, Hawkes E, Helms M, Hu D, Huang L, Huang S, Hunt C, Irschick D, Lin HT, Lingwall B, Marr A, Mazzolai B, Mcinroe B, Murthy T, O'hara K, Porter M, Sadek S, Sanchez M, Santamarina C, Shao L, Sharp J, Stuart H, Stutz HH, Summers A, Tao J, Tolley M, Treers L, Turnbull K, Valdes R, PAassenL vanViggiani G, Wilson D, Wu W, Yu X, Zheng J (2021) Bio-inspired geotechnical engineering: principles, current work, opportunities and challenges. Géotechnique. https://doi.org/10.1680/jgeot.20.P.170

- Mazzolai B, Meloni G, Degl'Innocenti A (2017) Can a robot grow? Plants give us the answer. In: Bioinspiration, Biomimetics, and Bioreplication 2017. SPIE, pp 24–33
- Migliaccio F, Tassone P, Fortunati A (2013) Circumnutation as an autonomous root movement in plants. Am J Bot 100:4–13. https://doi.org/10.3732/ajb.1200314
- 42. Minh NH, Cheng YP, Thornton C (2014) Strong force networks in granular mixtures. Granul Matter 16:69–78. https://doi.org/10.1007/s10035-013-0455-3
- Naclerio ND, Hubicki CM, Aydin YO, Goldman DI, Hawkes EW (2018) Soft robotic burrowing device with tip-extension and granular fluidization. In: 2018 IEEE/RSJ international conference on intelligent robots and systems (IROS), pp 5918–5923
- Plassiard J-P, Belheine N, Donzé F-V (2007) Calibration procedure for spherical discrete elements using a local moment law, pp 8
- Quillin KJ (2000) Ontogenetic scaling of burrowing forces in the earthworm *Lumbricus terrestris*. J Exp Biol 203:2757–2770. https://doi.org/10.1242/jeb.203.18.2757
- Sadeghi A, Tonazzini A, Popova L, Mazzolai B (2014) A novel growing device inspired by plant root soil penetration behaviors.
 PLoS ONE 9:e90139. https://doi.org/10.1371/journal.pone. 0090139
- 47. Sharif YU, Brown MJ, Ciantia MO, Cerfontaine B, Davidson C, Knappett J, Meijer GJ, Ball J (2021) Using discrete element method (DEM) to create a cone penetration test (CPT)-based method to estimate the installation requirements of rotary-installed piles in sand. Can Geotech J 58:919–935. https://doi.org/10.1139/cgj-2020-0017
- 48. Shi D, Yang Y, Deng Y, Xue J (2019) DEM modelling of screw pile penetration in loose granular assemblies considering the effect of drilling velocity ratio. Granul Matter 21:74. https://doi.org/10.1007/s10035-019-0933-3
- 49. Smilauer V, Angelidakis V, Catalano E, Caulk R, Chareyre B, Chèvremont W, Dorofeenko S, Duriez J, Dyck N, Elias J, Er B, Eulitz A, Gladky A, Guo N, Jakob C, Kneib F, Kozicki J, Marzougui D, Maurin R, Modenese C, Pekmezi G, Scholtès L, Sibille L, Stransky J, Sweijen T, Thoeni K, Yuan C (2021) Yade. Documentation. https://doi.org/10.5281/ZENODO.5705394
- Stamp NE (1984) Self-burial behaviour of Erodium cicutarium seeds. J Ecol 72:611–620. https://doi.org/10.2307/2260070
- Steendam C, Verhelst P, Van Wassenbergh S, De Meyer J (2020) Burrowing behaviour of the European eel (*Anguilla anguilla*): effects of life stage. J Fish Biol 97:1332–1342. https://doi.org/10. 1111/ifb.14481
- Tang Y, Huang S, Tao J (2020) Effect of rotation on seeds' selfburial process: insights from DEM simulations. In: Geo-Congress 2020. American Society of Civil Engineers, Minneapolis, Minnesota, pp 293–301
- Tao J (2021) Burrowing soft robots break new ground. Sci Robot-6:3615. https://doi.org/10.1126/scirobotics.abj3615
- Tao J, Huang S, Tang Y (2020) SBOR: a minimalistic soft selfburrowing-out robot inspired by razor clams. Bioinspir Biomim 15:055003. https://doi.org/10.1088/1748-3190/ab8754
- 55. Trueman ER (1966) The mechanism of burrowing in the polychaete worm, *Arenicola marina* (L.). Biol Bull 131:369–377. https://doi.org/10.2307/1539763
- Trueman ER, Brand AR, Davis P (1966) The dynamics of burrowing of some common littoral bivalves. J Exp Biol 44:469–492. https://doi.org/10.1242/jeb.44.3.469
- Trueman ER, Yonge M (1967) The dynamics of burrowing in Ensis (Bivalvia). Proc R Soc Lond B 166:459–476. https://doi. org/10.1098/rspb.1967.0007
- Vasko A (2020) An investigation into the behavior of ottawa sand through monotonic and cyclic shear tests. M.S., The George Washington University



- Wensrich CM, Katterfeld A, Sugo D (2014) Characterisation of the effects of particle shape using a normalised contact eccentricity. Granul Matter 16:327–337. https://doi.org/10.1007/ s10035-013-0465-1
- WinterDeits AGRLHV, Dorsch DS, Slocum AH, Hosoi AE (2014) Razor clam to RoboClam: burrowing drag reduction mechanisms and their robotic adaptation. Bioinspir Biomim 9:036009. https://doi.org/10.1088/1748-3182/9/3/036009
- Yang P, O'Donnell S, Hamdan N, Kavazanjian E, Neithalath N (2017) 3D DEM simulations of drained triaxial compression of sand strengthened using microbially induced carbonate precipitation. Int J Geomech 17:04016143. https://doi.org/10.1061/(ASCE)GM.1943-5622.0000848
- Zhong W, Liu H, Wang Q, Zhang W, Li Y, Ding X, Chen L (2021) Investigation of the penetration characteristics of snake skin-inspired pile using DEM. Acta Geotech 16:1849–1865. https://doi.org/10.1007/s11440-020-01132-2
- Zhou W, Yang L, Ma G, Xu K, Lai Z, Chang X (2017) DEM modeling of shear bands in crushable and irregularly shaped granular materials. Granul Matter 19:25. https://doi.org/10.1007/ s10035-017-0712-y

Publisher's Note Springer Nature remains neutral with regard to jurisdictional claims in published maps and institutional affiliations.

